

RESEARCH ARTICLE



WILEY

A collaborative framework for unifying typical multidimensional solar cell simulations – Part I. Ten common simulation steps and representing variables

Fa-Jun Ma¹ | Shaozhou Wang¹ | Chuqi Yi¹ | Lang Zhou² |
Ziv Hameiri¹ | Stephen Bremner¹ | Xiaojing Hao¹ | Bram Hoex¹

¹Australia Centre for Advanced Photovoltaics, School of Photovoltaic and Renewable Energy Engineering, University of New South Wales, Sydney, NSW, Australia

²Institute of Photovoltaics, Nanchang University, Nanchang, Jiangxi, China

Correspondence

Fa-Jun Ma, Australia Centre for Advanced Photovoltaics, School of Photovoltaic and Renewable Energy Engineering, University of New South Wales, Sydney, NSW 2052, Australia.

Email: f.ma@unsw.edu.au

Abstract

Multidimensional simulations for diverse solar cells often encounter distinctive configurations, even when employing the same simulation software. The complexity and inefficiency of this process are further exacerbated when employing different simulators. From our extensive decade-long experience in numerical simulations of diverse solar cells, we have identified ten common simulation steps intrinsic to typical electrical and optical simulations. Subsequently, we propose ten sets of variables that encompass all the relevant details required for these steps. To address the challenge of varying information requirements for each variable across different simulations, we assign a list, a versatile data type, to each variable. This approach, by design, enables concise, coherent, and flexible input, accommodating the unique demands of each simulation. However, to ensure unambiguous simulations, precise specifications for these variables are essential. Computer code has been successfully implemented to ensure adherence to specifications and expedite variable synchronization with Sentaurus, the de facto standard for device simulation. Within this framework, users are only tasked with editing variables in a plain text file, obviating the need for in-depth knowledge of Sentaurus. This streamlines the prerequisites for engaging in numerical simulation significantly. Through thoughtful design considerations, we preserve the simulation capacity while simultaneously enhancing productivity considerably. This open-source framework welcomes global collaboration within the photovoltaic community and has the potential to generate an extensive dataset for cost-effective artificial intelligence training.

1 | INTRODUCTION

Solar cells are semiconductor devices harvesting solar energy with the photovoltaic effect. Crystalline silicon (c-Si) solar cells have a ~ 95%

market share, and technologies like the passivated emitter and rear cell (PERC)¹ and tunnel oxide passivating contacts (TOPCon)² are dominating the market.³ Much like the biodiversity in nature, apart from c-Si cells, there exists a variety of single-junction

This is an open access article under the terms of the [Creative Commons Attribution-NonCommercial](https://creativecommons.org/licenses/by-nc/4.0/) License, which permits use, distribution and reproduction in any medium, provided the original work is properly cited and is not used for commercial purposes.

© 2024 The Authors. Progress in Photovoltaics: Research and Applications published by John Wiley & Sons Ltd.

high-performance solar cells, each with its unique advantages.⁴ Even for c-Si solar cells, there are several technological roadmaps, e.g. silicon heterojunction technology (HJT) solar cells achieve high performance by leveraging novel passivating contacts. Thin film cells like copper indium gallium selenide (CIGS) solar cells offer the advantages of low material consumption and fabrication cost. Emerging cells like perovskite solar cells hold the potential for achieving both high efficiency and cost-effective fabrication processes. Besides single-junction solar cells, multijunction solar cells, aiming to surpass the Shockley-Queisser limit,⁵ are also under investigation. For researchers in this field, innovation and investigation into diverse solar cell technologies are of paramount importance. This exploration typically involves a combination of experiments, characterizations, and numerical simulations. Numerical simulation has become an indispensable tool for advancing research in the field of solar cells, facilitating the understanding and optimization of these devices.⁶

In recent decades, there has been significant development in the field of device simulators for the study and optimization of silicon solar cells. Various free simulators, such as PC1D⁷ and Quokka,⁸ have emerged to enhance our understanding of silicon solar cell behavior. Additionally, simulators like AFORS-HET⁷ and SCAPS-1D⁸ are commonly utilized for thin-film solar technologies. However, it is important to note that these free simulators are designed for specific types of solar cells, and therefore, their applicability is limited to some extent. Commercial software packages like Sentaurus,⁹ Atlas,¹⁰ APSYS,¹¹ and COMSOL¹² are still widely employed in the photovoltaic community. While these commercial tools offer a more generic approach and theoretically can handle various solar cell technologies,

practical implementation often reveals dramatic differences in device setups for different types of solar cells, even when using the same simulator. This situation presents challenges for users. New users often encounter a steep learning curve when attempting to become proficient with these versatile simulators, while experienced users frequently find themselves reinventing solutions for specific solar cell configurations. Consequently, there is a lack of synergy in the photovoltaic community when it comes to unified multidimensional solar cell simulations, presumably due to the inherent difficulties in unifying simulations across diverse solar cell technologies.

The Excel spreadsheet originally developed by Altermatt¹³ in 1993, as depicted in the screenshot shown in Figure 1, has been a valuable resource for new users to initiate simulations with Sentaurus. The spreadsheet can generate input files for Sentaurus by specifying relevant parameters regarding simulation, geometry, etc. It has played a pivotal role in fostering a culture of expertise-sharing within the photovoltaic community. However, this spreadsheet was primarily tailored for conventional and PERC solar cell designs. Inspired by his pioneer work, we are motivated to create an open-source framework known as UniSolar. UniSolar has been designed to handle a broader spectrum of typical simulation tasks across various cell architectures and technologies, accommodating major simulation software. This framework is open to global collaboration, allowing for continuous improvements and enhancements. UniSolar has been actively under development since 2016, with initial concepts and designs being reported in 2018.¹⁴ Through numerous iterations, UniSolar has reached a level of maturity, and the most recent design details are presented in this article.

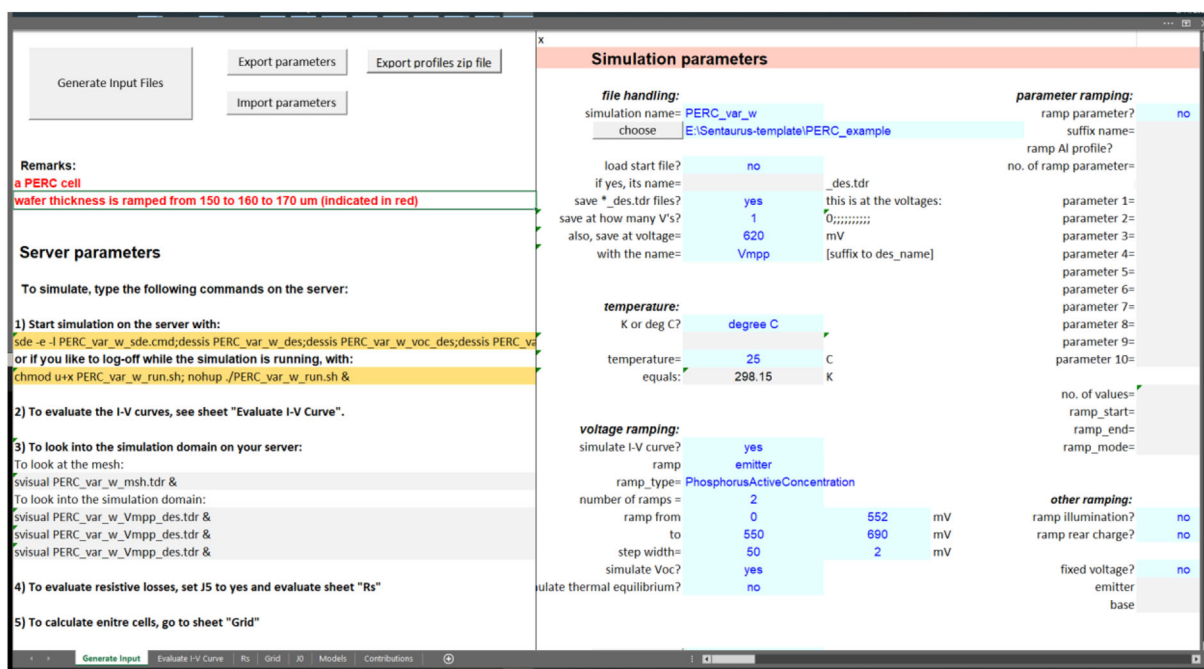


FIGURE 1 A screenshot of the excel spreadsheet created by Altermatt. At the main sheet, users could specify parameters related to simulation, geometrical cell, doping, quality, material, and photogeneration as well as batch settings and generate command files to be executed by Sentaurus.

In our systematic examination of a broad range of solar cell simulations using multiple simulators, we have identified a commonality in the form of ten distinct simulation steps. Notably, our work represents the initial effort to formalize these ten simulation steps into a comprehensive simulation workflow. For each of these individual simulation steps, we have devised a corresponding variable, conceived as structured lists, aimed at capturing the crucial and necessary particulars. To maintain a high degree of accuracy and uniformity, we have established precise specifications for each variable. We have implemented an independent grammar system that enforces adherence to these specifications and streamlines input. Additionally, we have integrated functionalities to facilitate variable synchronization with Sentaurus and have provided practical demonstrations of optical and electrical simulations. The UniSolar framework serves to enhance user control, elevate productivity, and introduce clarity and consistency into typical multidimensional solar cell simulations.

2 | TEN COMMON SIMULATION STEPS AND REPRESENTING VARIABLES

From 2009 to 2015, our research focus primarily revolved around device simulations related to various silicon-based solar cells such as conventional solar cells, PERC,¹⁵ all-back-contact, and HJT solar cells.¹⁶ With these simulations, we aimed to deepen our understanding of the operation and behavior of these solar cells to make informed design and optimization decisions. Additionally, we focused on optimizing material choices and device structures to achieve higher power conversion efficiency. Optical simulations¹⁷ were also

conducted to improve light trapping schemes. From 2015 onwards, our research expanded to encompass a broader range of solar cell technologies. This included solar cell types like TOPCon, carrier selective contacts,¹⁸ $\text{Cu}_2\text{ZnSnS}/\text{Se}_4$,¹⁹ perovskite,²⁰ III-V,²¹ tandem cells,²² etc. We employed numerical simulations to investigate and optimize the performance of these diverse solar cell architectures. Furthermore, we leveraged numerical simulations to simulate and understand various characterization techniques commonly used in solar cell research. These techniques included current density-voltage (J-V) characteristics, quantum efficiency (QE) measurements, quasi-steady-state photoconductance (QSSPC)²³ measurements for effective lifetime assessment,²⁴ Suns-open circuit voltage (Suns- V_{oc}) measurements, capacitance-voltage (C-V) measurements, photoluminescence analysis,²⁵ electroluminescence, etc.

Our simulations were conducted using a range of simulators, including Sentaurus, PC1D, Quokka, AFORS-HET, and SCAPS-1D. Throughout these simulations, we systematically explored and examined all the pertinent settings required for multidimensional electrical and optical simulations of solar cells. From a high-level perspective, we discerned a commonality in the simulation steps shared across these different tools. In Figure 2, we summarized the ten simulation steps involved in typical multidimensional optical and electrical simulations according to their rough sequence in a simulation workflow. In advanced simulators like Sentaurus, Step 1 'Simulation environment' needs to be specified to select the desired simulator version as well as which type of simulation to perform. This is crucial because electrical and optical simulations differ significantly in terms of the equations they solve and the scale of the unit cell. Additionally, if the simulator is only available on a remote server, one may need to specify which

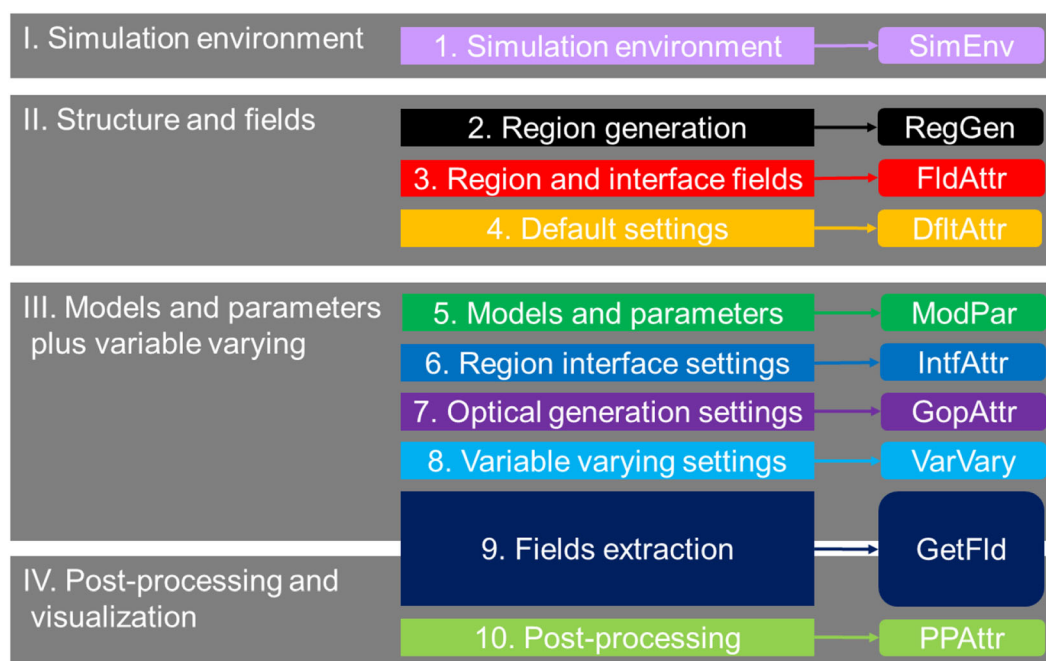


FIGURE 2 Typical multidimensional optical and electrical simulations of solar cells may be divided into four stages with ten sequential simulation steps that are well represented by ten corresponding variables.

scheduler (e.g. Portable Batch System, PBS) to use for coordinating computing resources for the simulation job. Additional parameters such as the number of CPUs, memory allocation, wall time, and other job-specific details may also be required depending on the nature of the simulation job. This step ensures that the simulation is executed using the appropriate software environment and resources.

To enhance the comprehension of Steps 2 to 10, PC1D is primarily employed to elucidate the precise purpose and scope of these nine steps. This choice is justified by the substantially broader user base of PC1D compared to Sentaurus. When examining a PC1D simulation, exemplified in Figure 3, it becomes evident that the relevant simulation parameters, which are applicable to any solar cell, can be generally classified into the same nine steps. With thoughtful design, as we extended from one-dimensional (1D) to two-dimensional (2D) or three-dimensional (3D) simulations and from basic to advanced simulation techniques using different simulators, these same nine steps remained sufficiently comprehensive to encompass all the pertinent simulation settings.

Solar cells exhibit a high degree of symmetry, allowing for a substantial simplification of their structure through the concept of a unit cell.²⁶ This practice proves invaluable in expediting simulations, especially under limited computing resources. In the context of electrical simulations, both surfaces are typically approximated as planar, sufficient for modeling carrier transport. Consequently, a full-size GaAsP/Si tandem cell, for example, can be represented as a 1D unit cell, as portrayed in Figure 4(a). Each layer in this unit cell corresponds to a single region and is represented as a line. However, when lateral carrier transport cannot be disregarded, the cell must be modeled as a 2D unit cell, as depicted in Figure 4(b). In this scenario, several layers are composed of multiple regions. The basic shape in this 2D representation takes the form of a rectangle or square, with the lateral width defined as the half-distance between two top metal fingers. To accurately capture the impact of bottom point contacts, the unit cell comprises 3D regions with the basic shape of a cuboid or cube, as exemplified in Figure 4(c). In the context of optical simulations, the surface texture of solar cells plays a pivotal role. As a result, the full-

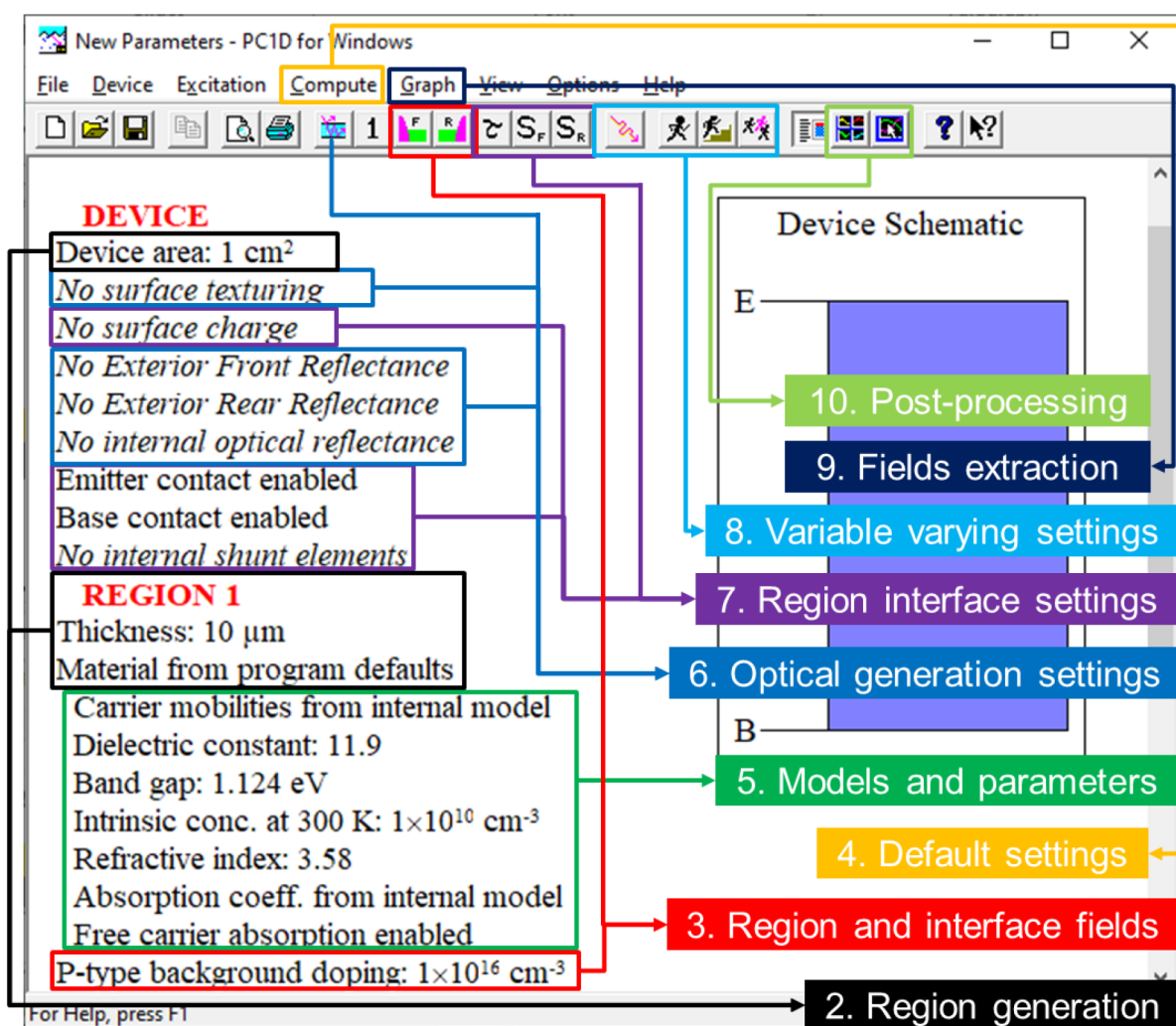


FIGURE 3 All the relevant settings in PC1D required to simulate a solar cell may be categorized into nine common simulation steps.

size cell can be effectively simplified to a unit cell comprising just one pyramid, as illustrated in Figure 4(d). Each unit cell forms a simulation domain and the domain (a few microns) in optical simulations is notably smaller than its counterpart (a few hundred microns) in 3D electrical simulations. Given the combined requirements of electrical and optical simulations, the 'region generation' step in Figure 3 must possess the capability to create both basic shapes and more intricate geometries, thereby accommodating the diverse demands of these simulations.

In PC1D, dopants are either uniformly set as background doping or strategically introduced into specific regions through both the top and bottom surfaces to ensure the proper functionality of solar cells. Expanding beyond the concept of dopants, we employ a more encompassing term, 'field', to include any spatial distribution of quantities that are relevant to the operation of solar cells. Within this broader definition, fields include but are not limited to dopants, charges, defects, and electron-hole pairs. Moreover, in the case of ternary and quaternary semiconductors, the mole fraction constitutes an essential field. In practice, dopants, defects, electron-hole pairs, and mole fractions are often directly specified as input fields for solar cells before simulations. Conversely, solar cells yield a multitude of output fields upon successful simulation completion, encompassing quantities such as carrier densities, recombination rates, etc. Notably among these output fields are band diagrams, providing valuable insights into the operation of solar cells under varying illumination and bias conditions. Based on the method of introduction, fields introduced into the background of the cell are defined as 'region fields', which are constant within a particular region. On the other hand, fields introduced from any region surface are categorized as 'interface fields'. These interface fields typically exhibit variations in depth from the interface, reflecting the intricacies of their spatial distribution. The 'Region and

interface fields' step in Figure 3 particularly refers to the introduction of input fields after establishing regions.

After delineating regions containing input fields, the generated unit cell undergoes subdivision into numerous non-uniform segments to effectively represent the spatial variability of input and output fields. This procedure is commonly referred to as mesh generation. Mesh generation plays a pivotal role in bridging the gap between mathematical models and real-world solar cells by providing the framework to represent complex geometries and numerically solve equations with precision. For example, the 'element size factor' influences the size of the elements in the mesh, which can be accessed through the 'Compute' menu in PC1D, as depicted in Figure 3. Additionally, PC1D offers a few other numerical parameters. These accessible parameters can differ among different simulators. It's worth noting that the default configurations in simulators are well-suited for most simulation scenarios. Adjusting these settings is typically recommended only for experienced users who have a deep understanding of the simulation process. Numerical settings pertaining to the calculation process are naturally incorporated within the 'Default settings' step in Figure 3.

In the context of electrical simulation, fully coupled Poisson, drift-diffusion, and carrier continuity equations²⁷ are solved iteratively until self-consistency is achieved. Within this computational framework, several key models like electron affinity, bandgap, density of states (DOS), and bandgap narrowing (BGN) have a significant influence on the band structure of a solar cell. Furthermore, mobility and recombination models play a pivotal role in shaping carrier transport and continuity equations. Specifically for Si, state-of-the-art models include the Schenk BGN,²⁸ Philips mobility,²⁹ Niewelt Auger,³⁰ radiative,³¹ and Shockley-Read-Hall (SRH) recombination^{32, 33} models. Moreover, the incomplete ionization model²⁸ is activated if

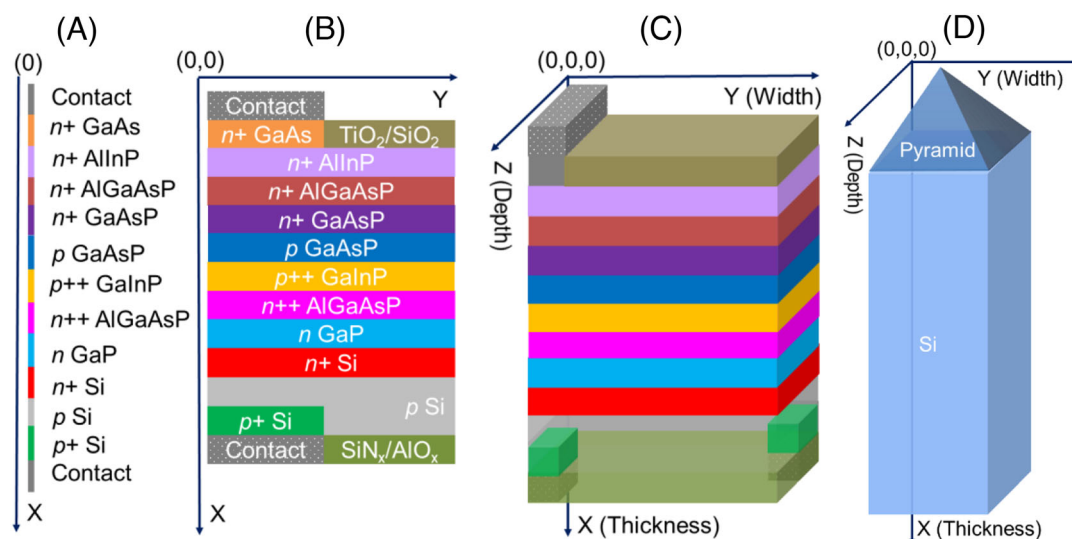


FIGURE 4 In electrical simulations, GaAsP/Si tandem solar cells can be simplified as (a) 1D, (b) 2D, and (c) 3D unit cells. In optical simulations, a solar cell can be reduced to (d) a 3D unit cell with just one pyramidal texture. In these unit cells, the coordinate system is consistent with different dimensions.

aluminum dopants are present in silicon regions, and the thermionic emission model is employed when heterointerfaces are identified in the unit cell, facilitating the calculation of currents and energy fluxes at these abrupt heterointerfaces. It is worth noting that while small surface textures like nanostructured black silicon surfaces³⁴ may reach quantum-mechanical length scales, quantization effects are not calculated since electrical simulations typically do not consider surface texture. Conversely, in the context of optical simulation, computation involves the propagation of light and the photogeneration in solar cells. This is accomplished by solving Maxwell's equations, or quite often, simplified models like raytracing. The results are typically determined by the complex refractive index of the regions involved in the simulation. Essential models and parameters influencing both electrical and optical behaviors are incorporated in the **'Models and parameters'** step as illustrated in Figure 3.

The **'Optical generation settings'** step plays a crucial role in influencing the spatial photogeneration within a solar cell by adjusting surface texture and altering boundary conditions at region interfaces, as illustrated in Figure 3. In Sentaurus, additional factors can be specified to enhance photogeneration, such as optimizing a top antireflective coating (ARC) and a bottom diffuse reflection. Optical and electrical simulations can be decoupled, especially when the photon recycling effect is weak, as is typically the case in silicon solar cells. The photogeneration profile can be calculated by the simulator itself or externally using an optical simulator and then imported into the chosen simulator for electrical simulations. This approach allows for the separation of optical and electrical aspects of a solar cell, streamlining the modeling process. It's worth noting that in many instances, solar cell behaviors are not highly sensitive to the precise spatial distribution of photogenerated carriers. This observation leads to the use of simplified modeling approaches like the Beer–Lambert law (e.g., in perovskite solar cells) or approximations employing analytical functions like an optical pathlength enhancement model.³⁴ These simplifications can expedite typical simulations while still providing reasonably accurate results for the behavior of the solar cell under various conditions.

Contacts serve the critical function of gathering photogenerated carriers. Additionally, they have associated series and shunt resistance affecting power output. Moreover, they are detrimental for excess carriers, underscoring the importance of passivated contacts in solar cell design. Imperfections in crystallinity and dangling bonds at the region interfaces can lead to strong interface recombination if not properly passivated. Techniques for mitigating interface recombination include a combination of field-effect passivation and chemical passivation.²⁴ Chemical passivation is determined implicitly by parameters like surface recombination velocities (SRVs) or explicitly through settings related to traps. Interface recombination can be suppressed by increasing surface charge and decreasing SRVs in PC1D. However, it's worth noting that the **'Region interface settings'** step in Figure 3 not only encompasses contact and interface configurations but also incorporates tunneling settings available in Sentaurus. Tunneling is often explored when studying carrier-selective contacts and multi-junction solar cells. Since tunneling is a nonlocal process, it is typically

associated with region interfaces, and its current is calculated based on the band edge profile between nonlocal mesh points.

Once the unit cell is generated and relevant settings are specified, it becomes possible to calculate the behavior of a solar cell under thermal equilibrium, where there is no net flow of thermal energy between regions. Parameters related to the unit cell size typically do not significantly deviate from thermal equilibrium, so they can be straightforwardly assigned the desired values. However, certain parameters such as bias voltage can introduce strong perturbations that make it difficult for the chosen simulator to converge if their values are directly assigned. Therefore, these parameters are practically set in the **'Variable varying settings'** step in Figure 3, allowing their values to be incrementally varied, either linearly or logarithmically, until the desired outcome is achieved. Solar cell simulations are often named after the characterization techniques they aim to mimic, such as light J-V or QE. Nevertheless, at their core, solar cell simulations essentially involve a series of discrete calculations under varying conditions. In this sense, as exemplified in Figure 5, typical solar cell simulations can be conducted by manipulating just four key parameters: spectrum intensity, monochromatic light intensity, monochromatic wavelength, and contact properties. Furthermore, it is feasible to execute multiple simulations in a single run by effectively managing variations in these four parameters. This approach allows for a comprehensive exploration of the solar cell's behavior across a range of conditions and scenarios.

Upon successful simulation completion, it is essential to interpret and gain insights from simulation results. In PC1D, users have access to 11 spatial fields like doping densities and energy bands through the **'Graph'** menu. These spatial fields are automatically extracted at each step and updated as the simulation progresses. In Sentaurus, users have the capability to save converged solutions under specific conditions to a structure file, somewhat akin to taking a snapshot during variable varying. Sentaurus also automatically extracts important characteristics, such as current and voltage on contacts, during variable varying. However, for more detailed knowledge of other output fields or to perform straightforward tasks like output field averaging and integration within a specific region or along a region interface, users

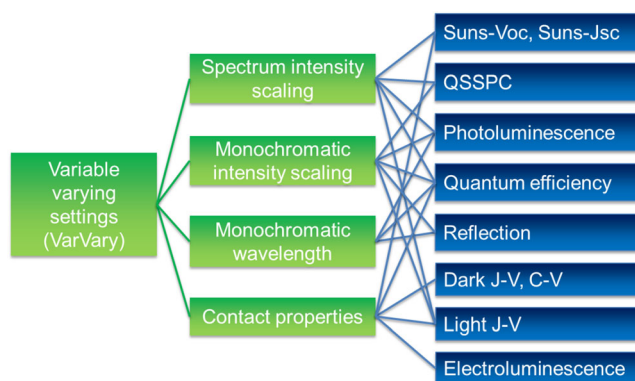


FIGURE 5 Typical optical and electrical simulations of solar cells, at their core, are variations of just four parameters.

can specify these settings in the 'Fields extraction' step. Furthermore, 1D cuts can be performed on each saved snapshot to obtain depth-dependent output field profiles, such as band diagrams. This step allows for a more comprehensive examination of simulation results.

PC1D offers a convenient 'four-graph view' button, as illustrated in Figure 3, that provides a quick overview of the spatial distribution of desired output fields and J-V. Similar visualization features are also found in other simulators for examining simulation results. The relevant settings for visualization are configured in the 'Post-processing' step. To analyze and characterize solar cell performance, predefined scripts are often available that can be executed to generate characteristic curves corresponding to well-known characterizations like light J-V and QE. Additionally, specific characteristic values can be extracted from calculated curves. For example, an excess carrier density of 10^{15} cm^{-3} is typically specified to obtain the effective minority carrier lifetime in a QSSPC simulation. Alternatively, one may choose to bypass pre-defined scripts and analyze raw data using external tools or methods if needed.

Advanced simulators like Sentaurus often employ multiple specialized tools/modules to perform various functions instead of relying on a single unified tool. In this context, the ten simulation steps may be categorized into four distinct stages in Figure 2 as follows:

- I. The initial stage focuses on setting up the general simulation environment.
- II. At stage II, the simulator generates the required unit cell and introduces relevant fields.
- III. At stage III, models are specified, parameters are set for regions and interfaces, and variables are varied as needed for the simulation.
- IV. The final stage involves post-processing and visualization of simulation results.

To the best of our knowledge, we are the first to formalize the ten simulation steps and document this simulation workflow, thereby providing a structured framework for conducting simulations of solar cells. This structured framework has proven to be a pioneering contribution, offering clarity and consistency in typical multidimensional solar cell simulations. It has streamlined the simulation process, fostering more efficient research and development endeavors in the field.

Ten variables have been meticulously formulated to correspond to the ten simulation steps delineated in Figure 2. These variables have been devised to comprehensively furnish the requisite information for the precise and coherent execution of solar cell simulations. To accommodate varying information requirements, every variable has been intentionally designed to be interpreted as a list in this work, which enables concise and coherent input for both simple and complex solar cell simulations. In the realm of computer science, a list is a data structure consisting of an ordered sequence of values and settings. In the Tool Command Language (Tcl), lists are typically represented by enclosing the space-separated values and settings within braces, thereby constituting a flat list. It's important to underscore

that lists as a data type are highly flexible and dynamic. They can take on various forms, such as:

- Empty list: {} – A list with no elements.
- Single-element list: {Sentaurus} or Sentaurus – Braces are optional in this case.
- Multiple-element flat list: {Sentaurus T-2022.03 !Cylindrical Optical PBS 18 20 4}
- Nested list: A list containing one or more elements, where one or more of these elements are also lists.
- Single-element nested list with an empty list: {}{} – A list has one element which is an empty list.

Compared to traditional variables that typically hold a single value, using lists offers significant advantages in modeling complex multidimensional solar cells. Lists allow for the efficient organization of numerous pertinent settings and values within a single variable, reducing the need for many separate variables. Particularly, a nested list provides a powerful way to organize and structure data, allowing for the encapsulation of multiple sublists with their corresponding details. This approach not only simplifies data management but also minimizes the chances of errors when editing individual settings.

Precise variable specifications are critical to eliminate ambiguity and maintain coherence in solar cell simulations. Each variable in the simulation workflow has well-defined specifications that align seamlessly with its previously described purpose and scope. These specifications are essential because they establish clear criteria for acceptable values within each element of a list. Detailed and up-to-date specifications can be found in the 'COMMENT' section associated with each variable in the plain [variable file](#). It's important to note that specifications may undergo minor revisions as part of future development efforts. However, the utmost care will be taken to ensure backward compatibility so that existing variable files remain functional even with updated specifications. This commitment to compatibility is essential for maintaining the integrity and reliability of the UniSolar framework.

3 | COMPREHENSIVE DESIGN OF 'REGGEN' AND 'FLDATTR'

The 'RegGen' variable describing the 'Region generation' step stands as a critical cornerstone within the UniSolar framework. It is essential to delve into additional design considerations to ensure a coherent generation of both simple and intricate geometries. The comprehensive design insights provided here are aimed at fostering a thorough understanding of region generation, complementing the formal specifications outlined in the variable file. 'Region generation' is particularly challenging in the context of unifying multidimensional solar cell simulations for two primary reasons: Firstly, disparities and variations from one simulation to another are often most pronounced in this variable as solar cell technologies continually evolve, leading to innovations in cell structure and design. The flexibility to accommodate

various cell structures and configurations is essential to address these challenges effectively. Secondly, a few subsequent variables within the simulation workflow rely heavily on the accurate and consistent specification of regions. Any inaccuracies or inconsistencies in region specifications can potentially lead to errors and inaccuracies in the simulation results.

To generate regions that can be used seamlessly across simulations, it is important to introduce a unified coordinate system, which is illustrated through the following three scenarios. As shown in Figure 4(a), a full-size GaAsP/Si tandem cell can be modeled as a 1D unit cell. In this scenario, only the X-axis is used, originating from the top point of the cell, and pointing toward the bottom. When lateral carrier transport is not negligible, the cell must be modeled as a 2D unit cell in Figure 4(b). In this configuration, the Y-axis is introduced, originating from the top left corner of the unit cell, and extending to the right, while the X-axis remains consistent with the 1D case. To account for the impact of bottom point contacts and more complex 3D effects, 3D regions must be generated as shown in Figure 4(c). In this case, the Z-axis is added to the coordinate system, originating from the furthest point of the top left edge, and running towards us. The X and Y axes are retained as in the 2D case. This unified coordinate system offers the advantage of consistency, where each region has its thickness in the X-direction, width in the Y-direction, and depth in the Z-direction, irrespective of the dimensions and complexity of the simulation. In addition, all regions are situated within the positive axes of the coordinate system with the top left further corner of the unit cell serving as the origin point.

In most electrical simulations, every region in 3D is usually a cuboid or can be subdivided into multiple cuboids. In this context, it is practical to describe each region unambiguously by providing its composing material followed by its thickness, width, and depth values. This implicit method simplifies the spatial definition of regions without the need to explicitly specify their vertices. However, to ensure accurate and unique region definition, three fundamental rules must be followed: the **sequence rule**, the **division rule**, and the **omission rule**.

- i. **Sequence rule:** Regions should be enumerated in a specific order, starting from the topmost to bottom layers, from the leftmost to right sections within each layer, and from the furthest to nearest regions within each section.
- ii. **Division rule:** This rule serves as a prerequisite for the sequence rule. It dictates that a region must be subdivided if it spans multiple layers or multiple sections.
- iii. **Omission rule:** This rule is crucial to handle situations where multiple regions exist within the same layer or section in 2D/3D simulations. It demands that a region should omit specifying its thickness if it shares its layer with the previous region. Furthermore, if the previous region and the current region are within the same section, the region should skip specifying both its thickness and width.

By adhering to these three rules—**sequence**, **division**, and **omission**—users can generate regions accurately and seamlessly, starting

from the origin and extending towards the positive axes. For most solar cell structures, regions are deposited layer by layer and can be listed sequentially without subdividing any region. However, some unique cell structures may not satisfy the prerequisite of the sequence rule due to their inherent complexity or unconventional geometries. In these cases, the **division rule** should be applied first to accommodate the structure's complexity. For example, in Figure 6(a), laser ablation was performed to create a recess region for isolating the electron and hole contacts in an all-back-contact solar cell. In this configuration, two contacts and thin film layers beneath are not situated in the same layer. It is necessary to create more layers by dividing the cell perpendicular to the X-axis, as indicated by those horizontal lines. After the division, regions are indexed from 1 to N according to the sequence rule for easy reference later. The indexing convention used is that 'r#' refers to a specific region, while 'r#/#' denotes a region interface, with '#' representing the region index. Notably, conductors and metals are typically simplified to surface contacts in simulations, so materials like ITO and metal contacts are not individually indexed. To ensure the final simulation domain remains rectangular, dummy air regions (e.g., 'r6', 'r9', 'r11', 'r13') are included in the simulation domain.

In Figure 6(b), the CZTSe structure³⁵ consists of two layers of grains. In the top layer, the width of the furthest grain is the sum of the other two. To accurately represent this structure, the furthest grain in the top layer is divided into two regions (e.g., 'r3' and 'r5'), as indicated by the plane along the 'r4/6' interface. To sum up, the **division rule** stipulates that a region should not span multiple layers or multiple sections. In practical applications, the minimum number of layers is determined from top to bottom, with the counter increasing as soon as one encounters the bottom face or edge of a region. Similarly, the minimum number of sections within a layer is determined from left to right, with the counter increasing as soon as one finds the right face or edge. These three rules together with the specification in the variable file help ensure consistent and accurate region definitions, even in complex solar cell structures.

In optical simulations, and occasionally in electrical simulations, there is a need to model special shapes that cannot be easily represented by rectangles/cuboids. In such cases, the implicit method alone is not sufficient to overcome this challenge. To accurately model these complex surface textures or shapes, it becomes necessary to define them explicitly by providing coordinates or vertices. This explicit method allows for the creation of 2D and 3D shapes that go beyond basic geometries. In the explicit method, several 2D and 3D special shapes can be defined, as shown in Figure 7(a). In 2D simulations, any closed shape can be created using a polygon. In 3D simulations, four special shapes can be assigned to regions: an ellipsoid/sphere, a cuboid/cube, a pyramid, and a cone/cylinder.

To manage potential conflicts between the implicit and explicit methods, two rules are established: the **domain rule** and the **old-replaces-new rule**. The **domain rule** specifies that only the implicit method can determine the simulation domain. Unlike the implicit method, regions specified by the explicit method may overlap with existing regions. In such cases, the **old-replaces-new rule** states

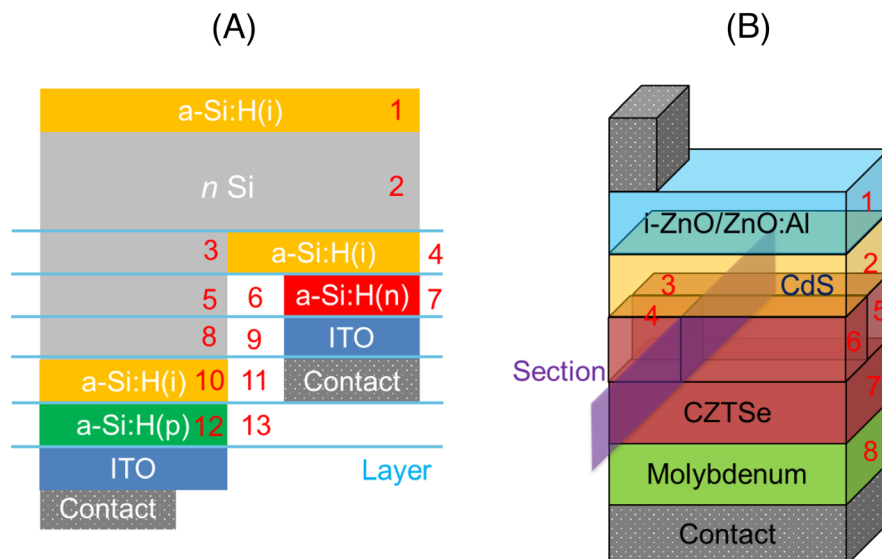


FIGURE 6 Schematic illustration for applying the division and sequence rules to two different types of cells: (a) 2D unit cell of an all-back-contact solar cell, where horizontal lines indicate additional layers created, and (b) 3D unit cell of a CZTSe solar cell, where the vertical rectangle denotes an additional section created.

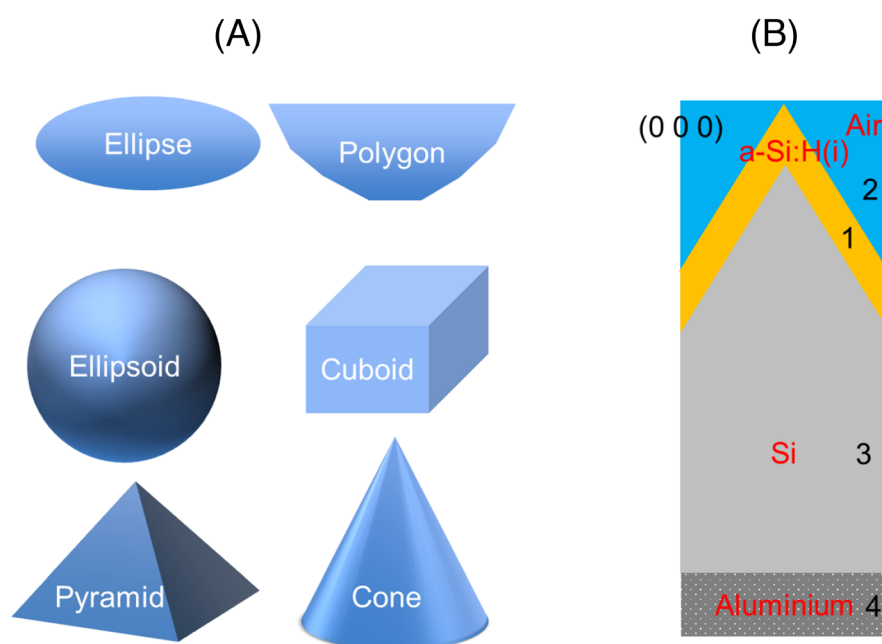


FIGURE 7 (a) Typical 2D and 3D shapes supported by the explicit method; (b) a cross-sectional view of a silicon substrate with pyramidal texture and a thin layer of intrinsic hydrogenated amorphous silicon a-Si:H(i) on top, which are generated with a combination of the explicit and implicit methods.

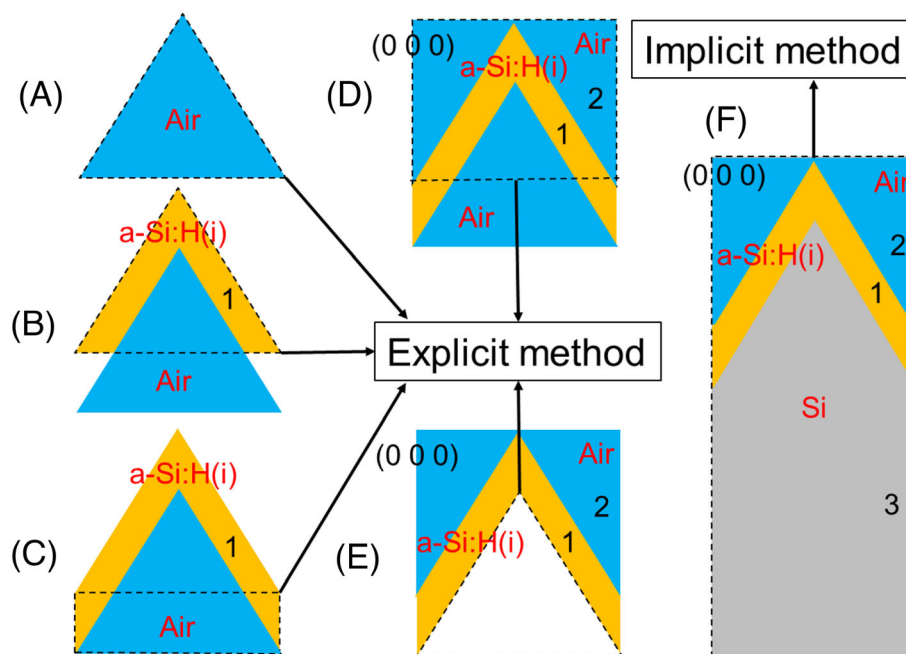
that any overlapping region should be subtracted from the newly generated shape. With these two rules in place, it is essential to use the explicit method before the implicit method. If part of a shape falls outside of the simulation domain, it will be automatically removed, allowing users to create the desired surface topology while ensuring the simulation remains within the specified domain. This combination of implicit and explicit methods offers flexibility in modeling complex cell geometries in solar cell simulations.

In some cases, the surface topology of a solar cell may be quite complex and cannot be represented by a single special shape. To handle such situations, users have the flexibility to create intricate geometries by combining multiple shapes. Additionally, users can manage each shape created with the explicit method by choosing from three actions: **keep**, **remove**, and **merge**.

- **Keep:** Selecting the 'keep' action preserves the drawn shape at the end of the explicit method.
- **Remove:** The 'remove' action discards the drawn shape at the end of the explicit method.
- **Merge:** The 'merge' action combines the drawn shape with the previous shape, effectively uniting them into a single region. This can be useful when creating complex structures that involve multiple shapes.

For example, consider the 2D cross-section of a prototypical unit cell featuring upright pyramids and a top intrinsic hydrogenated amorphous silicon (a-Si:H(i)) passivation layer, as shown in Figure 7(b). Figure 8 demonstrates how to use a combination of explicit and implicit methods to accurately model this complex structure. Here's a

FIGURE 8 A cross-sectional view of detailed steps to draw the structure in Figure 7(b): (a) draw a dummy upright pyramid composed of air with the action, **remove**; (b) draw an upright pyramid composed of a a-Si:H(i) with the action, **keep**; (c) draw a cuboid composed of a-Si:H(i) with the action, **merge**; (d) draw a cuboid composed of air with the action, **keep**; (e) remove the dummy pyramid after the explicit method; (f) draw the Si substrate with the implicit method.



step-by-step breakdown of the process with dashed edges denoting the boundaries of the drawn shape at each step:

- Figure 8(a): It begins by drawing a dummy pyramid.
- Figure 8(b): Subsequently, a pyramid composed of a $a\text{-Si:H(i)}$ material is introduced to create region 'r1'. The overlapping region with the dummy pyramid is removed from region 'r1'.
- Figure 8(c): Further, a cuboid composed of $a\text{-Si:H(i)}$ is incorporated and merges into region 'r1'. Again, any overlap region with the dummy pyramid is eliminated from region 'r1'.
- Figure 8(d): A cuboid composed of air creates region 'r2'. The overlapping regions with the existing region 'r1' and the dummy pyramid are removed from region 'r2'.
- Figure 8(e): At this step, the explicit method reaches its end, and any region marked for removal is taken away. In this case, the dummy pyramid is removed.
- Figure 8(f): Region 'r3' is generated from the origin using the implicit method. Given the prior existence of regions 'r1' and 'r2', region 'r3' encapsulates the combined geometries of the pyramid and cuboid, adhering to the old-replaces-new rule.
- Bottom region: After drawing the bottom cuboid region 'r4' composed of aluminum material, the complete 3D unit cell, as shown by the 2D cross-section in Figure 7(b), is established in the chosen simulator.

This approach allows users to create intricate and realistic surface topologies accurately representing the solar cell's structure and properties. It combines both explicit and implicit methods to handle complex geometries efficiently. A unit cell may be generated with different combinations and users possess the flexibility to determine the most effective way to generate the necessary regions.

With an established unit cell, all the region interfaces are readily referenced. Yet, any region surface at the simulation domain boundary is not the case. To overcome this limitation, particularly in electrical simulations, dummy air layers are introduced to comprehensively encompass the simulation domain. These dummy layers ensure that all region surfaces are accessible and well-defined. Here's how they are implemented in different simulation dimensions in electrical simulations:

- 1D: Two dummy layers are created: One to the top, indexed as 0. The other is to the bottom, indexed as $N + 1$.
- 2D: Two additional dummy layers are generated than the 1D case: One to the left, indexed as $N + 2$. The other to the right is indexed as $N + 3$. If cylindrical coordinates are employed, only one additional dummy layer is created to cover the right side, indexed as $N + 2$.
- 3D: Two more dummy layers are introduced than the 2D case: One to the furthest side, indexed as $N + 4$. The other to the opposite side, indexed as $N + 5$.

In optical simulations, regardless of the dimensions, only the top dummy layer is created to enable referencing the top surface. With the inclusion of dummy layers, the final simulation domain always takes a rectangular or cuboidal shape. Yet, users possess the flexibility to create the unit cell or the active simulation domain of various shapes.

The variable 'FldAttr' representing the '**Region and interface fields**' step introduces input fields to regions. While region interfaces are typically denoted implicitly as 'ri/]', they can also be explicitly represented using the coordinates of two opposite vertices. These vertices are identified using a specific indexing convention, such as

'pA' or 'px_y_z', where 'A' denotes a vertex, and 'x', 'y', and 'z' denotes the X, Y, and Z coordinates, respectively. An explicit interface is defined by specifying two vertices from 'A' to 'B', denoted as 'pA/B' or 'px1_y1_z1/px2_y2_z2'. When introducing interface fields, a depth profile is placed along the normal vector V_n originating from the region interface. For implicit interfaces, 'ri/j' indicates that V_n points from region i to region j, while 'rj/i' signifies the reverse direction. For explicit interfaces, determining V_n requires **special notations** in 1D and the application of the **right-hand rule** in 2D/3D. The **right-hand rule** involves extending the thumb, index, and middle fingers perpendicular to each other and is applied differently in 2D and 3D scenarios.

- 1D: As depicted in Figure 9(a), **special notations** 'pA/+' and 'pA/-' are used to distinguish V_n .
- 2D: As illustrated in Figure 9(b), the **right-hand rule** always points the middle finger to the positive Z-axis. For the interface 'pA/B', the thumb points from vertex 'A' to 'B', and the index finger designates V_n . Similar methods apply to other interfaces like 'pB/C', 'pC/D', and 'pD/A'.
- 3D: As exemplified in Figure 9(c), the **right-hand rule** always aligns the thumb with X, the index with Y, and the middle with Z. Furthermore, it is necessary to project the line between two vertices to the corresponding axes. For the interface 'pA/C', it is divided into 'pA/B' and 'pA/D', and V_n is determined by aligning the index from 'A' to 'B' and the middle from 'A' to 'D'. The same rule applies to the rest of the interfaces.

Notably in 3D, the order of vertices does not affect the determination of V_n , meaning that 'pA/C' is equivalent to 'pC/A' when calculating V_n for explicit interfaces. Explicit interfaces are useful and more accurate in some cases. For example, each depth profile is associated with a lateral Gaussian decay factor to account for lateral diffusion. To prevent lateral diffusion within multiple adjacent region interfaces with the same depth profile, the entire interface should be explicitly specified with its two opposite vertices.

4 | DEMONSTRATION

After laying out specifications for ten sets of variables, strict adherence to these specifications is reinforced by implementing a novel and independent grammar system. The grammar system comprises multiple small rule checks that can be linked together to ensure compliance with even intricate specifications. Importantly, this system offers the flexibility to adapt to changes in specifications without the need for coding adjustments. Instead, only the rule chains in the variable file (at the 'GRAMMAR' section of each variable) need to be updated. The grammar check process for each variable is executed in four passes and incorporates additional features such as case-insensitivity, autocomplete functionality, and the ability to reuse previously entered input. These features collectively simplify the input process, leading to a clear and concise presentation of simulation setup information. Our streamline approach facilitates the presentation of input values of multidimensional solar cell simulations in a single table for publication. This approach with ten sets of variables may help researchers consistently report their simulation setups in the future.

After editing the plain variable file, the simulation process is initiated or halted using a script file that serves as the central control mechanism. This script file handles all the essential tasks, encompassing grammar check, variable conversion, Sentaurus command file generation, and job execution/termination. In addition to the primary script file, there are two auxiliary script files specifically designed for saving/restoring simulation-related files. These auxiliary files handle the task of saving and restoring relevant files to and from a Tar/GZip archive. This functionality allows for efficient preservation and verification of simulation outcomes and rapid incubation of new simulations. This well-structured approach enhances the organization and reproducibility of simulation processes, streamlining research efforts and ensuring the integrity of results. In forthcoming papers, we will report the design of the grammar system and the integration specifics of bidirectional synchronization with Sentaurus.

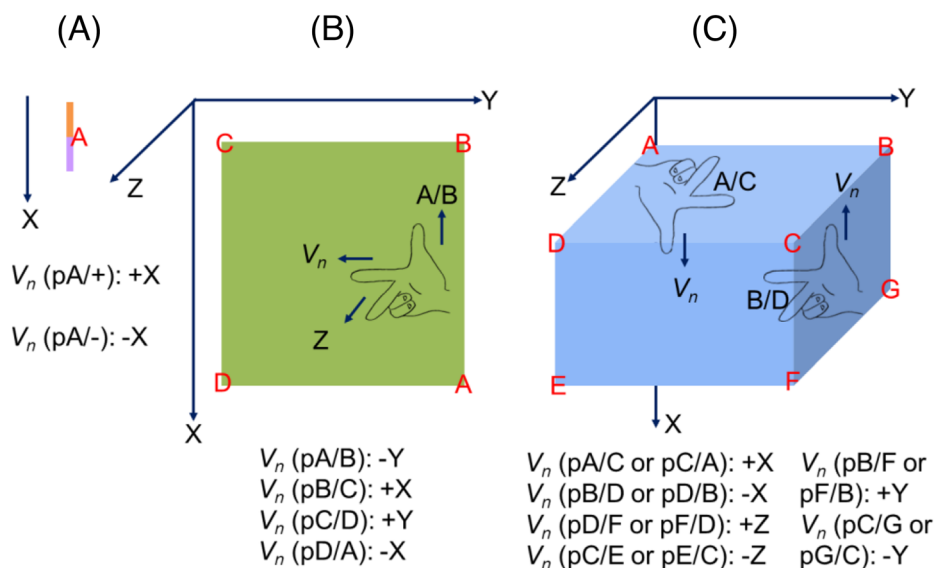


FIGURE 9 The normal vector V_n for an explicit interface is determined by (a) **special notations** in 1D and the **right-hand rule** in (b) 2D and (c) 3D.

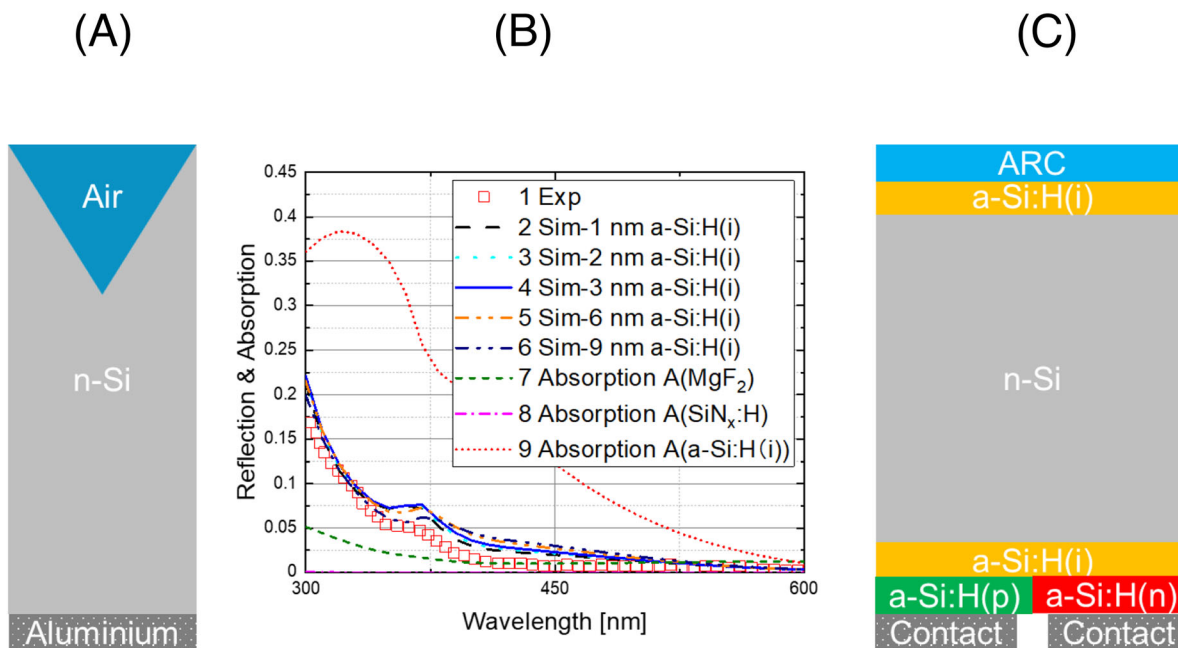


FIGURE 10 A silicon HJT solar cell with interdigitated back contacts³⁶: (a) unit cell for optical simulation; (b) simulated and measured reflection curves plus absorption in each top thin-film layer when a-Si:H(i) is 6 nm; (c) unit cell for electrical simulations.

The HJT solar cell with interdigitated back contacts has been reported to achieve an impressive power conversion efficiency of 26.3%.³⁶ Based on the revealed details in this reference and reasonable assumptions, both optical and electrical simulations with ten sets of variables were performed to replicate the reported reflection, QE, and light J-V curves. For optical simulations, a cross-sectional representation of the unit cell with a textured top surface and a simplified bottom (neglecting thin film layers) is depicted in Figure 10(a). From the reference, a layer of a-Si provides the top surface passivation. For best chemical passivation, this layer should be a-Si:H(i). While the specifics of the ARC stack were not disclosed in the reference, it is very likely that hydrogenated silicon nitride ($\text{SiN}_x\text{:H}$) was deposited atop a-Si:H(i). In addition to light trapping, this $\text{SiN}_x\text{:H}$ layer serves as a hydrogen source and provides the necessary field-effect passivation to complement the a-Si:H(i) layer, which will be discussed in electrical simulations.

Based on the agreement observed for wavelengths below 600 nm as demonstrated in Figure 10(b), the top texture is identified to consist of inverted pyramids with a slant angle of 54.74° . The base length of these pyramids is assumed to be 5 μm . The ARC stack is fitted to be 90 nm MgF_2 ³⁷ and 70 nm $\text{SiN}_x\text{:H}$ with a refractive index of 1.92 at 633 nm.¹⁷ According to the agreement for wavelengths from 1,000 nm to 1,200 nm (not shown), the bottom diffuse reflection was characterized by a Phong factor of 1 (Lambertian surface) and a broadband reflectivity of 0.93. However, the exact thickness of the top a-Si:H(i) layer cannot be determined through optical simulations. Various simulations were conducted with a-Si:H(i) thickness ranging from 1 to 9 nm, yielding comparable results indicated by curves 2 to 6. It is worth mentioning that during a-Si:H(i) deposition, the undesired crystalline silicon epitaxial growth can negatively impact

TABLE 1 Input values for performing reflection, absorption, and transmission (RAT) simulation. Detailed explanations of each variable can be found in Appendix A.

Variable	Value
SimEnv	{Sentaurus T-2022.03 !Cylindrical Optical PBS 18 20}
RegGen	{{Gas Pyramid Keep p0_0_0/3.53610857633_0_0 54.74} {Silicon 165 2.5 2.5} {Aluminum 1 2.5 2.5}}
FldAttr	{{r2 P 1.56e15}}
IntfAttr	{}
GopAttr	{{p0_0_0/0_2.5_2.5 Raytrace 5,000 Deterministic} {r1/2 ARC MgF2 0.09 01mdb/MgF2_1988Siqueros.par SiNx 0.07 01mdb/SiNx_1.92_SERIS.par iaSi 0.001 01mdb/a- Si-i_2015Ling.par} {r3/2 0.93 Phong 1} {monochromatic 0.3 1e-3}} 0/1/-1=0.002 0/1/-1=0.003 0/1/ -1=0.006 0/1/-1=0.009
DfltAttr	{{Mesh 10 0.05 8 0.001 8 1.5 0.001 1.1} {Numeric 64} {Other 25}}
ModPar	{{r2 01mdb/Si_298.15K_2022Green.par} {r3 01mdb/ Al_1985Palik.par}}
VarVary	{{Monoscaling 1} {Wavelength 1.2 90}}
GetFld	{}
PPAttr	{{v1 RAT}}

passivation quality.³⁸ This effect might explain the reported thickness dependence of lifetime samples passivated by a-Si:H(i).³⁹ Notably, the thickness of the top a-Si:H(i) layer was reported to be 6 nm on the world-record 26.81% HJT solar cell.⁴⁰ It is rational to set the top a-Si:H(i) thickness to 6 nm for the subsequent electrical simulations. Curves 7 to 9 in Figure 10(b) illustrate detailed light absorption in

MgF₂, SiN_x:H, and 6 nm a-Si:H(i), respectively. MgF₂ exhibits low broadband absorption except for wavelengths below 350 nm and above 1,050 nm (not shown), with an AM1.5G weighted absorption current density of 0.76 mA/cm². The low refractive index SiN_x:H is transparent while the 6 nm a-Si:H(i) displays strong absorption for wavelengths below 600 nm, with an AM1.5G weighted absorption current density of 1.22 mA/cm². All the input values for the ten sets of variables are detailed in Table 1.

Electrical simulations were carried out on the unit cell illustrated in Figure 10(c) under standard test conditions, aiming to provide insights into its performance and efficiency. The following assumptions were used in these simulations. The distance between the bottom electron contacts is assumed to be 100 μ m. The width ratio

TABLE 2 Input values for conducting QE and light J-V simulations. Detailed explanations of each variable can be found in Appendix B.

Variable	Value
SimEnv	{Sentaurus T-2022.03 !Cylindrical Electrical PBS 1 5}
RegGen	{{iasi 0.006 50} {silicon 165 50} {iaso 0.006 50} {pasi 0.02 45} {nasi 5} {gas 0.1 44.5} {gas 1} {gas 4.5}}
FldAttr	{{r2 P 1.56e15} {r4 B 1.41e19} {r5 P 1.45e19}}
IntfAttr	{{r4/6 c0} {r5/8 c1} {r0/1 1e12 1e5} {r4,5/7 0 1e7} {r1,3/2 0 430}} 0/2/1,2=0/0
GopAttr	{{r0/1 external 02opt/HJT_165um_a-Si-i_6nm_Spectral.plx} {spectrum 02opt/am1.5g_IEC60904-3_2008.txt 0.3 1.2 0.01} {monochromatic 0.3 1e-3}}
DfltAttr	{{Mesh 10 0.05 8 0.001 8 1.5 0.001 1.1} {Numeric 64} {Other 25}}
ModPar	{{r2 01mdb/Si_298.15K_2022Green.par SRH 0.0088 Aug Niewelt 0.55} {r1,3 01mdb/a-Si-i_2015Ling.par SRH ! Trap 03exp/Traps/Bulk_a-Si-i_2015Ling.txt} {r4 01mdb/a-Si-p_2015Ling.par SRH ! Trap 03exp/Traps/Bulk_a-Si-p_2015Ling.txt} {r5 01mdb/a-Si-n_2015Ling.par SRH ! Trap 03exp/Traps/Bulk_a-Si-n_2015Ling.txt}}
VarVary	{{Specscaling 0.3} {Monoscaling 1 1} {Wavelength 1.2 90} {Monoscaling 0} {Specscaling 1} {c0 0.8 160}}
GetFld	{{p5_0/160_50 Average Dn} {p0_20&0_48 1 2 Band}}
PPAttr	{{v2 QE} {v5 JV}}

between boron doped a-Si:H(p) and phosphorus-doped a-Si:H(n) is set to 9:1. The doped a-Si:H layers are assumed to have a thickness of 20 nm.⁴⁰ The gap between the hole and electron contacts is taken as 1 μ m. Regarding field-effect and chemical passivation, the low refractive index SiN_x:H is assigned a typical fixed charge density (Q_f) of 10^{12} q/cm² and the SRV between SiN_x:H and a-Si:H(i) is set to 10^5 cm/s. The a-Si:H(i) layer is assumed to provide identical chemical passivation for the top and bottom surfaces, with an SRV of 190 cm/s. Interface recombination between a-Si:H(i) and doped a-Si:H layers is neglected. The outer surface of doped a-Si:H is considered unpassivated, with an SRV of 10^7 cm/s. The SRH lifetime in the n-type substrate is set to 8.8 ms according to the reference [36]. The SRH recombination in three types of a-Si:H is calculated explicitly based on traps, following a previous simulation study.¹⁶ The photon recycling fraction in the substrate is calculated to be 0.55 assuming good light trapping properties.³⁰ QE and light J-V characteristics were simulated in one run using detailed input values for the ten sets of variables specified in Table 2.

Figure 11 indicates that measured QE and light J-V characteristics can be reasonably reproduced with the previously assumed parameters. Curve 5 in Figure 11(a) is calculated by removing reflection and absorption in ARC, which is the theoretical upper limit of the external QE. Strikingly, curve 5 closely aligns with the measured external QE, suggesting that the internal QE within the silicon substrate and the top a-Si:H(i) layer is close to 100%, up to a wavelength of 1,000 nm. This observation challenges the conventional assumption that most photogenerated electron-hole pairs are rapidly recombined within a-Si:H(i). This assumption is primarily rooted in the understanding that a-Si:H(i) is very defective, leading to SRH lifetimes as low as picoseconds. Curve 4, on the other hand, is computed by further subtracting the absorption in 6 nm a-Si:H(i) from curve 5. The difference between curve 4 and the measured QE below 600 nm is remarkable, suggesting effectively suppressed recombination due to efficient charge carrier separation and injection into the substrate, which was already characterized by photoluminescence.^{41, 42}

The negligible recombination observed in a-Si:H(i) can be attributed to the field-effect passivation of SiN_x:H. SiN_x:H possesses a high-density fixed positive charge, which induces a strong electric field within a-Si:H(i) as well as the surface region of the substrate. The

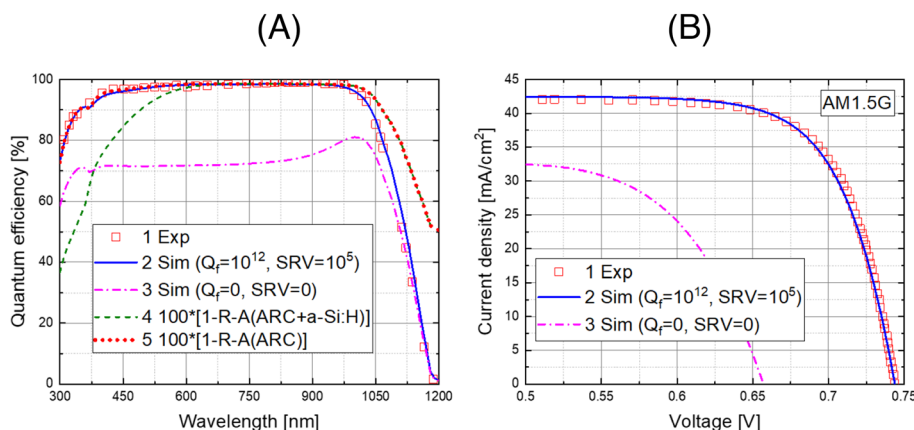


FIGURE 11 (a) Measured and simulated QE, and (b) light J-V of silicon HJT solar cell with interdigitated back contacts for two scenarios: SiN_x:H and perfect chemical passivation with zero fixed charge density.

induced electric field in a-Si:H(i) facilitates charge carrier separation and hole transport towards the substrate. This field effect prevents photogenerated carriers from recombining rapidly within a-Si:H(i), even in the presence of high-density defects. This field effect also reduces the interface recombination between $\text{SiN}_x\text{:H}$ and a-Si:H(i) to negligible levels. In essence, $\text{SiN}_x\text{:H}$'s field-effect passivation plays a crucial role in suppressing recombination and outweighs the adverse impact of high-density traps within the a-Si:H(i) layer. It is worth noting that $\text{SiN}_x\text{:H}$ not only provides field-effect passivation to a-Si:H(i) but also extends its passivation to the top a-Si:H(i)/Si interface. When field-effect passivation is absent (i.e. Q_f is zero), external QE is significantly lower, as exemplified by curve 3 in Figure 11(a). This QE reduction is due to increased recombination occurring at the top a-Si:H(i)/Si interface. These observations are further supported by the results presented in curve 3 of the light J-V simulation in Figure 11(b). These results emphasize the critical role of applying strong field-effect passivation to the top a-Si:H(i) layer. Essentially, $\text{SiN}_x\text{:H}$ provides strong field-effect passivation, both within the top a-Si:H(i) layer and at its interface with the substrate. This insight highlights the significance of proper field-effect passivation in optimizing the performance of this solar cell.

5 | SUMMARY

Our research has uncovered ten universal simulation steps in typical multidimensional optical and electrical simulations of diverse solar cells. UniSolar was created to include ten sets of variables, proposed to describe all the relevant details required by these ten simulation steps. All variables were set to take lists as their values to enable concise, coherent, and flexible input. We further established precise specifications for each variable to avoid unambiguity. Through practical demonstrations, we have showcased that advanced optical and electrical simulations can be executed efficiently using these ten sets of variables, without the complexities often associated with sophisticated simulators like Sentaurus. UniSolar is poised to revolutionize the modeling process, making it more accessible to a wider audience and reducing the entry barriers for numerical simulations. It promises to enhance the predictive capabilities and productivity within the photovoltaic research community, ultimately contributing to advancements in solar cell technology.

ACKNOWLEDGEMENTS

Without many iterative improvements, this work will never reach its present status. F.-J. Ma appreciates the following students and staff providing feedback on the development of UniSolar: Aobo Pu, Jing Zhao, Hongzhao Li, Mengjie Li, Alexander To, Zhenyu Sun, Yuchao Zhang, Udo Roemer, Yansong Wang, Ruimeng Wang. The authors highly appreciate the constructive comments and suggestions from reviewers to enhance the scientific quality of this manuscript. Additionally, GPT-3.5 was used to improve the readability of this manuscript and all simulations were performed on the Katana high-performance computing cluster (doi: [10.26190/669x-a286](https://doi.org/10.26190/669x-a286)). Open access

publishing facilitated by University of New South Wales, as part of the Wiley - University of New South Wales agreement via the Council of Australian University Librarians.

CONFLICT OF INTEREST STATEMENT

Authors are responsible for the content and declare that they have no conflict of interest.

DATA AVAILABILITY STATEMENT

The Tar/GZip files for the demonstrated optical and electrical simulations are accessible under 07tpl/01demo/PartI on the UniSolar GitHub repository.

ORCID

Fa-Jun Ma  <https://orcid.org/0000-0002-9373-2213>

Shaoshou Wang  <https://orcid.org/0000-0002-7299-3481>

Chuiqi Yi  <https://orcid.org/0000-0002-5518-5941>

REFERENCES

1. Min B, Muller M, Wagner H, et al. A roadmap toward 24% efficient PERC solar cells in industrial mass production. *IEEE J Photovolt*. 2017; 7(6):1541-1550. doi:[10.1109/JPHOTOV.2017.2749007](https://doi.org/10.1109/JPHOTOV.2017.2749007)
2. Richter A, Benick J, Müller R, et al. Tunnel oxide passivating electron contacts as full-area rear emitter of high-efficiency p-type silicon solar cells. *Prog Photovolt*. 2018;26(8):579-586. doi:[10.1002/ppp.2960](https://doi.org/10.1002/ppp.2960)
3. International Technology Roadmap for Photovoltaic (ITRPV), Twelfth Edition. Twelfth. 2021. <http://www.itrs.net/Links/2013ITRS/2013Chapters/2013Litho.pdf>
4. NREL. Best Research-Cell Efficiency Chart 2021. (accessed December 6, 2021) <https://www.nrel.gov/pv/cell-efficiency.html>
5. Shockley W, Queisser HJ. Detailed balance limit of efficiency of p-n junction solar cells. *J Appl Phys*. 1961;32(3):510-519. doi:[10.1063/1.1736034](https://doi.org/10.1063/1.1736034)
6. Zhao J, Wang A, Altermatt P, Green MA. Twenty-four percent efficient silicon solar cells with double layer antireflection coatings and reduced resistance loss. *Appl Phys Lett*. 1995;66(26):3636-3638. doi:[10.1063/1.114124](https://doi.org/10.1063/1.114124)
7. Clugston DA, Basore PA. PC1D version 5: 32-bit solar cell modeling on personal computers. 26th IEEE Photovoltaic Specialists Conference - 1997, IEEE. n.d.:207-10. doi:[10.1109/PVSC.1997.654065](https://doi.org/10.1109/PVSC.1997.654065)
8. Fell A. A free and fast three-dimensional/two-dimensional solar cell simulator featuring conductive boundary and quasi-neutrality approximations. *IEEE Trans Electron Devices*. 2013;60(2):733-738. doi:[10.1109/TED.2012.2231415](https://doi.org/10.1109/TED.2012.2231415)
9. "Sentaurus TCAD." Synopsys Inc., Sunnyvale, CA, 2023. Accessed: Sep. 10, 2023. [Online]. Available: <https://www.synopsys.com/manufacturing/tcad.html>
10. "Victory TCAD." Silvaco, Inc., Santa Clara, CA. 2023. Accessed: Sep. 10, 2023. [Online]. Available: <https://silvaco.com/tcad/>
11. "APSYS." Crosslight Software Inc., Vancouver, BC. 2019. Accessed: Sep. 10, 2023. [Online]. Available: <https://crosslight.com/products/apsys/>
12. Nardone M, Green B. COMSOL-PV : A Unified Platform for Numerical Simulation of Solar Cells and Modules. 2015 COMSOL Conference. 2015.
13. Altermatt PP. Sentaurus input-file generator 2023. (accessed September 10, 2023). <https://www.pvlighthouse.com.au/cms/simulation-programs/sentaurus-input-file-generator>
14. Ma F-J, Zhao J, Yi C, Pu A, Hameiri Z. A unified parameter set designed for typical 2D/3D simulations of homo-/hetero-/single-/multi-junction solar cells in various simulation programs.

- 2018 IEEE 7th World Conference on Photovoltaic Energy Conversion (WCPEC) (A Joint Conference of 45th IEEE PVSC, 28th PVSEC & 34th EU PVSEC), IEEE. 2018:3190–3193. doi:10.1109/PVSC.2018.8548198
15. Ma F-J, Liu H, Liao B, et al. Impact of auger recombination parameterisations on predicting silicon wafer solar cell performance. *J Comput Electron*. 2014;13(3):647–656. doi:10.1007/s10825-014-0583-y
 16. Ling ZP, Duttagupta S, Ma F-J, Mueller T, Aberle AG, Stangl R. Three-dimensional numerical analysis of hybrid heterojunction silicon wafer solar cells with heterojunction rear point contacts. *AIP Adv*. 2015;5(7):077124. doi:10.1063/1.4926809
 17. Duttagupta S, Ma F-J, Hoex B, Mueller T, Aberle AG. Optimised anti-reflection coatings using silicon nitride on textured silicon surfaces based on measurements and multidimensional modelling. *Energy Procedia*. 2012;15:78–83. doi:10.1016/j.egypro.2012.02.009
 18. Zhao J, Ma FJ, Ding K, et al. Advanced interface modelling of n-Si/HNO₃ doped graphene solar cells to identify pathways to high efficiency. *Appl Surf Sci*. 2018;434:102–111. doi:10.1016/j.apsusc.2017.10.163
 19. Pu A, Ma F, Yan C, et al. Sentaurus modelling of 6.9% Cu₂ZnSnS₄ device based on comprehensive electrical & optical characterization. *Sol Energy Mater sol Cells*. 2017;160:372–381. doi:10.1016/j.solmat.2016.10.053
 20. Ho-Baillie A, Zhang M, Lau CFJ, Ma F-J, Huang S. Untapped potentials of inorganic metal halide perovskite solar cells. *Joule*. 2019;3(4):938–955. doi:10.1016/j.joule.2019.02.002
 21. Gupta B, Shehata MM, Lee Y, et al. Unveiling the role of H₂ plasma for efficient InP solar cells. *Solar RRL*. 2023;7(6):2200868. doi:10.1002/solr.202200868
 22. Zheng J, Lau CFJ, Mehrvarz H, et al. Large area efficient interface layer free monolithic perovskite/homo-junction-silicon tandem solar cell with over 20% efficiency. *Eng Environ Sci*. 2018;11(9):2432–2443. doi:10.1039/C8EE00689J
 23. Sinton RA, Cuevas A, Stuckings M. Quasi-steady-state photoconductance, a new method for solar cell material and device characterization. Proceedings of the 25th IEEE Photovoltaic Specialists Conference (PVSC), IEEE. 1996:457–60. doi:10.1109/PVSC.1996.564042
 24. Ma F-J, Samudra GG, Peters M, et al. Advanced modeling of the effective minority carrier lifetime of passivated crystalline silicon wafers. *J Appl Phys*. 2012;112(5):054508. doi:10.1063/1.4749572
 25. Ma F-J. Advanced numerical modeling and simulation of silicon wafer solar cells. PhD thesis. National University of Singapore. 2013. <https://scholarbank.nus.edu.sg/handle/10635/77715>
 26. Altermatt PP. Models for numerical device simulations of crystalline silicon solar cells—a review. *J Comput Electron*. 2011;10(3):314–330. doi:10.1007/s10825-011-0367-6
 27. Green MA. *Solar cells: operating principles, technology and system applications*. UNSW Photovoltaics; 1982.
 28. Schenk A. Finite-temperature full random-phase approximation model of band gap narrowing for silicon device simulation. *J Appl Phys*. 1998;84(7):3684–3695. doi:10.1063/1.368545
 29. Klaassen DBM. A unified mobility model for device simulation—I. Model equations and concentration dependence. *Solid State Electron*. 1992;35(7):953–959. doi:10.1016/0038-1101(92)90325-7
 30. Niewelt T, Steinhäuser B, Richter A, et al. Reassessment of the intrinsic bulk recombination in crystalline silicon. *Sol Energy Mater sol Cells*. 2022;235:111467. doi:10.1016/j.solmat.2021.111467
 31. Fell A, Niewelt T, Steinhäuser B, Heinz FD, Schubert MC, Glunz SW. Radiative recombination in silicon photovoltaics: modeling the influence of charge carrier densities and photon recycling. *Sol Energy Mater sol Cells*. 2021;230:111198. doi:10.1016/j.solmat.2021.111198
 32. Shockley W, Read WT. Statistics of the Recombinations of holes and electrons. *Phys Rev*. 1952;87(5):835–842. doi:10.1103/PhysRev.87.835
 33. Hall RN. Electron-hole recombination in germanium. *Phys Rev*. 1952;87(2):387–387. doi:10.1103/PhysRev.87.387
 34. Wang S, Scardera G, Ma F-J, et al. Quantifying the effect of Nanofeature size on the electrical performance of Black silicon emitter by nanoscale modeling. *IEEE J Photovolt*. 2022;12(3):744–753. doi:10.1109/JPHOTOV.2022.3148713
 35. Li J, Huang J, Ma F-J, et al. Unveiling microscopic carrier loss mechanisms in 12% efficient Cu₂ZnSnSe₄ solar cells. *Nat Energy*. 2022;7(8):754–764. doi:10.1038/s41560-022-01078-7
 36. Yoshikawa K, Kawasaki H, Yoshida W, et al. Silicon heterojunction solar cell with interdigitated back contacts for a photoconversion efficiency over 26%. *Nat Energy*. 2017;2(5):17032. doi:10.1038/nenergy.2017.32
 37. Siqueiros JM, Machorro R, Regalado LE. Determination of the optical constants of MgF₂ and ZnS from spectrophotometric measurements and the classical oscillator method. *Appl Optics*. 1988;27(12):2549–2553. doi:10.1364/AO.27.002549
 38. Chu F, Qu X, He Y, et al. Prediction of sub-pyramid texturing as the next step towards high efficiency silicon heterojunction solar cells. *Nat Commun*. 2023;14(1):3596. doi:10.1038/s41467-023-39342-3
 39. Deligiannis D, Marioleas V, Vasudevan R, Visser CCG, van Swaaij RACMM, Zeman M. Understanding the thickness-dependent effective lifetime of crystalline silicon passivated with a thin layer of intrinsic hydrogenated amorphous silicon using a nanometer-accurate wet-etching method. *J Appl Phys*. 2016;119(23):235307. doi:10.1063/1.4954069
 40. Lin H, Yang M, Ru X, et al. Silicon heterojunction solar cells with up to 26.81% efficiency achieved by electrically optimized nanocrystalline-silicon hole contact layers. *Nat Energy*. 2023;8(8):789–799. doi:10.1038/s41560-023-01255-2
 41. Paduthol A, Juhl MK, Nogay G, Löper P, Trupke T. Measuring carrier injection from amorphous silicon into crystalline silicon using photoluminescence. *Prog Photovolt*. 2018;26(12):968–973. doi:10.1002/pp.3042
 42. Paduthol A, Juhl MK, Nogay G, Löper P, Ingenito A, Trupke T. Impact of different capping layers on carrier injection efficiency between amorphous and crystalline silicon measured using photoluminescence. *Sol Energy Mater sol Cells*. 2018;187:55–60. doi:10.1016/j.solmat.2018.07.016

How to cite this article: Ma F-J, Wang S, Yi C, et al. A collaborative framework for unifying typical multidimensional solar cell simulations – Part I. Ten common simulation steps and representing variables. *Prog Photovolt Res Appl*. 2024; 32(5):330–345. doi:10.1002/pp.3779

APPENDIX A

In-depth explanations are provided herein to facilitate comprehension of the input settings outlined in Table 1 for optical simulation, as follows:

- **SimEnv:** Optical simulation is conducted without the cylindrical coordinate and is carried out using the Sentaurus T-2022.03 version. The simulation task is managed by the PBS system, allocating a maximum CPU time of 18 hours and a memory capacity of 20 GB.
- **RegGen:** A silicon substrate, 165 μm in thickness, is generated with a top inverted pyramidal texture covering one-quarter of its surface and a bottom aluminum contact. For the inverted pyramid, its slant angle is 54.74° , its base center and vertex are located at (0, 0, 0) and (3.53610857633, 0, 0), respectively.
- **FldAttr:** The substrate has a phosphorus active concentration of $1.56 \times 10^{15} \text{ cm}^{-3}$.
- **GopAttr:** Initial optical simulation employs a monochromatic wavelength of 0.3 μm and an intensity of 0.001 W/cm^2 . The raytracing method is employed with a total of 5,000 initial rays under deterministic mode. Light interference effects are computed for an ARC stack comprising 0.09 μm MgF_2 , 0.07 μm SiN_x , and a-Si:H (i) toward the substrate, with a-Si:H(i) thickness varying at 1, 2, 3, 6, and 9 nm. Optical properties of each thin film are specified in the subsequent parameter file. Bottom diffuse reflection is characterized by the Phong model with a Phong factor of 1 and a broad-band reflectivity of 0.93.
- **DfltAttr:** Solar cell temperature is set at 25°C . Floating-point number precision in simulation is controlled with 64 bits. Region refinement stipulates a minimum space of 8 for every dimension, with maximum and minimum element sizes limited to 10 and 0.05 μm , respectively. Interface refinement involves the creation of at least 8 interface layers with a minimum layer thickness of 1 nm and an expansion ratio of 1.5. Optical refinement dictates a minimum layer thickness of 1 nm and an expansion ratio of 1.1.
- **ModPar:** Material and model properties of the substrate and bottom contact are defined in the corresponding material parameter file.
- **VarVary:** Monochromatic light intensity is ramped up from 0 to 1 (0.001 W/cm^2). Wavelength is ramped up from 0.3 to 1.2 μm with 90 intervals.
- **PPAttr:** For the second ramping step in 'VarVary,' a predefined script is executed to compute spectral reflection, absorption, and transmission.

APPENDIX B

Detailed elucidations are provided below to help understanding the input settings presented in Table 2 for electrical simulation:

- **SimEnv:** Electrical simulation is conducted without the cylindrical coordinate and is carried out using the Sentaurus T-2022.03

version. The simulation task is managed by the PBS system, allocating a maximum CPU time of 1 hour and a memory capacity of 5 GB.

- **RegGen:** A silicon substrate is created with a thickness of 165 μm and a width of 50 μm . The top and bottom are symmetrically covered by 6 nm a-Si:H(i). The bottom a-Si:H(i) layer is further covered on the left side by a-Si:H(p) with a width of 45 μm and on the right side by a-Si:H(n) with a width of 5 μm . Dummy layers on the left and right have widths of 44.5 μm and 4.5 μm , respectively. The middle dummy layer has a thickness of 0.1 μm and a width of 1 μm .
- **FldAttr:** The substrate has a phosphorus active concentration of $1.56 \times 10^{15} \text{ cm}^{-3}$. The a-Si:H(p) layer is boron-doped to $1.41 \times 10^{19} \text{ cm}^{-3}$ and the a-Si:H(n) layer is phosphorus-doped to $1.45 \times 10^{19} \text{ cm}^{-3}$.
- **IntfAttr:** Contacts on a-Si:H(p) and a-Si:H(n) are designated as c0 and c1, respectively. Fixed charge and SRV between a-Si:H(i) and the substrate are set to 0 q/cm^2 and 430 cm/s , respectively. Non-contacted surfaces of a-Si:H(p) and a-Si:H(n) are set to 0 q/cm^2 and 10^7 cm/s . Top surface passivation of the top a-Si:H(i) layer has two scenarios: a) 10^{12} q/cm^2 and 10^5 cm/s , and b) 0 q/cm^2 and 0 cm/s .
- **GopAttr:** Initial monochromatic wavelength is set to 0.3 μm with its intensity of 0.001 W/cm^2 . The illumination spectrum is AM1.5G, ranging from 0.3 to 1.2 μm with a step size of 10 nm. Spectral 1D photogeneration is loaded from the solution of the previous optical simulation.
- **DfltAttr:** Solar cell temperature is set at 25°C . Floating-point number precision in simulation is controlled with 64 bits. Region refinement stipulates a minimum space of 8 for every dimension, with maximum and minimum element sizes limited to 10 and 0.05 μm , respectively. Interface refinement involves the creation of at least 8 interface layers with a minimum layer thickness of 1 nm and an expansion ratio of 1.5. Optical refinement dictates a minimum layer thickness of 1 nm and an expansion ratio of 1.1.
- **ModPar:** Material and model properties of the substrate and a-Si:H layers are defined in the corresponding material parameter file. The substrate has a SRH lifetime of 8.8 ms. The Auger recombination in the substrate is calculated with the Niewelt equation and the photon recycling factor is set to 0.55. SRH recombination in each a-Si:H layer is calculated explicitly based on traps defined in the respective files.
- **VarVary:** Sequentially, spectrum intensity is ramped up from 0 to 0.3 (0.03 W/cm^2), monochromatic light intensity from 0 to 1 (0.001 W/cm^2), and wavelength from 0.3 to 1.2 μm with 90 intervals. Monochromatic light intensity is ramped down from 1 to 0. Spectrum intensity is ramped up from 0.3 to 1 (0.1 W/cm^2), and the voltage at contact c0 is ramped from 0 to 0.8 V at 160 intervals.
- **GetFld:** Extract and calculate the average excess carrier density in the substrate. Extract 1D band diagram at Y values of 20 and 48 μm from the saved snapshots.
- **PPAttr:** For the third ramping step in 'VarVary,' run the predefined script to calculate QE. For the last ramping step, run the predefined script to calculate light J-V characteristics.